Non-conjugated electrochromic supercapacitors with atom-economic arylamine-based AB$_2$-polyamides†

Yu-Jen Shao,[a] Yi-Ju Cho,[a] Hou-Lin Li,[a] Chien-Chieh Hu[*b] and Guey-Sheng Liou [ID] [*a]

A highly atom-economic AB$_2$-type hyperbranched polyamide (**HPA**) derived from arylamine monomers was judiciously designed and prepared. This electroactive **HPA** was further end-capped with two different end-cappers to prepare **HPA-B** and **HPA-TPA** with intrinsic microporous structures, which exhibited improved counter-ion diffusivity in electrochemical processes. With the aid of the intrinsic microporous structure, **HPA-TPA** revealed outstanding characteristics such as three-stage color changes, the highest coloration efficiency (CE), and the shortest switching response times among the prepared redox-active polyamides. Electrochromic devices employing **ECD-HPA-TPA** in this study demonstrated remarkable performance, evidenced by their rapid coloration rate of 27.4% s^{-1} and impressive switching stability. While evaluating and comparing the capacitive behavior of the **HPA-TPA** film, it showed 73.2 F g^{-1} at 1.0 A g^{-1} with nearly 60% transmittance contrast with only 220 nm thickness, and stability with 90.2% retention in a 300-cycle charge–discharge process. Furthermore, we compared its stability with polyamides derived from triphenylamine-based diamines to elucidate the effect on the reversibility during the charge–discharge process.

Introduction

Electrochromic (EC) materials have caught the world's eye because they handily achieve spectral absorption changes in visible and near-infrared regions upon the electrochemical redox process.[1,2] Meanwhile, electrochromic devices (ECDs) have demonstrated promising applications in several fields, such as smart windows, anti-glare mirrors, energy-saving displays, portable electronics, and supercapacitors.[3–7] Desirable ECDs should feature a high colour contrast ratio, remarkable coloration efficiency, a short response time, long-term stability, and polyelectrochromic capability. Among the conventional organic EC materials, triarylamine-derived monomers or polymers exhibited notable features and potential owing to their reversible redox characteristics, electron-rich nitrogen centres, and easy-to-modify nature.[8,9] These polymers typically exhibit a high optical contrast ratio, transforming the appearance from transparency at the neutral state to different colours during redox processes. However, increasing the polymer film thickness to obtain high optical contrast is inevitable, significantly increasing the response time and suppressing the

EC stability, thereby substantially influencing the EC behavior.[10] To deal with the dilemma issue of the EC behaviour effectively, introducing a porous structure into polymer films to increase the surface area and channels could facilitate the enhancement of the diffusivity of counter-ions within the film, resulting in a lower oxidation potential, shorter response time, and higher EC stability.[11] The most straightforward strategy was to utilize electrolyte salts to occupy polymer film space and wash them out.[12] However, this approach caused large porosity in the film, presenting the worst optical transparency at the neutral state and lower transmittance change. Apart from using electrolyte salts, making polymers of intrinsic microporosity (PIM) films by introducing bulky and twisted conformation has been proposed to enhance the diffusivity of counter-ions within the film during the electrochemical process. The incorporation of bulky and twisted moieties such as pentiptycene or Tröger's base creates intrinsic microporosity in the polymer matrix to promote the specific surface area and the diffusion of counter-ions within the polymer matrix, which facilitates switching capability while maintaining high transparency at the neutral state.[13,14]

Hyperbranched polymers (HPs) are also preferable candidates for obtaining an intrinsic microporous architecture composed of dendritic, linear, and terminal units randomly distributed among polymer matrixes.[15–17] Compared to linear polymers, HPs demonstrate peculiar characteristics such as high solubility, low density, and tuneable end groups while lacking significant entanglement.[18] HPs typically could be synthesized *via* one-pot polymerization using monomers

[a]*Institute of Polymer Science and Engineering, National Taiwan University, No. 1, Sec. 4, Roosevelt Rd., Taipei 10617, Taiwan. E-mail: gsliou@ntu.edu.tw*

[b]*Graduate Institute of Applied Science and Technology, National Taiwan University of Science and Technology, Taipei 106335, Taiwan. E-mail: cchu@mail.ntust.edu.tw*

containing A_xB_y (x or $y \geq 2$) reactive functional groups.[19] The outstanding advancement subsequently garnered interest in hyperbranched polymers to develop in various fields such as drug delivery, dispersion, coating, gas separation membranes, and supercapacitors.[20–24] Besides, the degree of branching (DB) is a crucial parameter to differentiate their structures to tune the void feature by the degree of linear, branched, and terminal segments.[25] Meanwhile, when considering a highly atom-economic approach in preparing EC materials, the HPs are suitable for using the A_xB_y architecture to design and maximize the content of electroactive units within the polymer matrix.[26]

Recently, advanced EC applications have tried to merge the energy-storage function into EC materials such as electrochromic supercapacitors (ESC)[14,27–30] or electrochromic batteries (ECB),[31–35] and these materials generally could be classified as inorganic and organic categories. Once we focused on the polymeric electrode materials, conjugated polymeric materials, especially by the electro-deposited method, spring up and have been widely used recently due to the highly π-conjugated main chain structure and the intrinsic mesoporosity generated during the electrochemical polymerization to perform higher specific capacitance (C_{sp}) and the durability. Very recently, we have proposed a judicious approach that the triarylamine-based non-conjugated polyamides could also reveal outstanding charge–discharge characteristics with high C_{sp} values (the highest can reach 165.3 F g^{-1}) and remarkable optical contrasts (ΔT) on two-stage colour changes.[14] So far, the non-conjugated polymeric electrode materials have attracted the attention of researchers for development and investigation in these two years.[29,30,36,37] Constantin et al. introduced phenoxazine (POZ) chromophores into the triphenylamine moiety to prepare a non-conjugated linear polyamide, and the resulting POZ-incorporated polyamide showed high ΔT contrast, remarkable C_{sp}, and good stability.[30] At the same time, they also mentioned that the thickness of the polyamide film results in a trade-off relationship between electrochromism and supercapacitor performance.

Herein, we propose an AB$_2$-type hyperbranched polyamide (**HPA**) synthesized by phosphorylation polyamidation reactions of the AB$_2$-type monomer N,N-bis(4-aminophenyl)-N′-(4-carboxyphenyl)-N′-(4′-methoxyphenyl)-1,4-phenylenediamine with different end-capping agents, benzoic acids (**BA**) and 4-carboxy-4′,4″-dimethoxytriphenylamine (**TPA**), for **HPA-B** and **HPA-TPA**,

respectively (Scheme 1). The obtained cavity-rich hyperbranched polyamides could increase more intrinsic microporous than linear polymers to suppress ion entrapment, promoting a faster response time and higher stability. Besides, the structural design of the methoxy group as a protecting group attached at the *para* position of a phenyl ring facilitates the enhancement of electrochemical and EC stability. Herein, we suppose that the hyperbranched **HPA-TPA** polyamide could reveal enhanced diffusivity, multicoloured characteristics, faster response times, outstanding electrochemical stability, and remarkable charge–discharge characteristics for advanced ESC applications.

Results and discussions

Characterization and basic properties of monomers and polyamides

The novel AB$_2$-type monomer N,N-bis(4-aminophenyl)-N′-(4-carboxyphenyl)-N′-(4′-methoxyphenyl)-1,4-phenylenediamine (**TPPA-AB$_2$**) and the AB-type monomer N,N′-bis(4-methoxyphenyl)-N-(4-carboxyphenyl)-N′-(4-aminophenyl)-1,4-phenylenediamine (**TPPA-AB**) were prepared *via* nucleophilic substitution and Ullman reactions, following the alkaline hydrolysis and reduction reactions, as shown in Scheme S1,† and the detailed synthetic routes are described in the Experimental section and ESI.† NMR spectroscopy, FT-IR spectroscopy, and high-resolution electrospray ionization mass spectrometry (HREIMS) were performed to characterize the obtained intermediates and target monomers, as illustrated in Fig. S1–S14.† The FT-IR spectra of the resulting compounds **3**, **4**, and **TPPA-AB$_2$** monomer are depicted in Fig. S1.† Compound **3** showed the characteristic band of the primary amino stretching at 3433 and 3350 cm^{-1}. After the nucleophilic substitution reaction, compound **4** exhibited two distinct bands of the nitro group at around 1590 and 1310 cm^{-1} for asymmetric and symmetric stretching with the disappearance of the primary amino signals. After hydrolysis and reduction reactions, the absorption peaks associated with the cyano (2220 cm^{-1}) and nitro groups vanished in the **TPPA-AB$_2$** spectrum; instead, the primary amino group absorption appeared at 3440 and 3355 cm^{-1}, and the C=O and the broad O–H stretching absorptions for the carboxylic acid group appeared at 1680 cm^{-1} and 2700 to 3400 cm^{-1} range, respectively. To confirm the structure of **TPPA-AB**, the FT-IR spectra of intermediate compounds **5**, **6**, and the **TPPA-AB** monomer are depicted in Fig. S2.† Compound **5** exhibited typical absorptions of the secondary amino stretching at 3315 cm^{-1}, the cyano group at 2215 cm^{-1}, and the nitro stretching at around 1590 and 1310 cm^{-1}. Compound **6** confirmed the disappearance of the secondary amino group after the Ullmann reaction to functionalize the anisole moiety, maintaining the cyano characteristic peak. After the hydrolysis and hydrogenation reactions, the **TPPA-AB** monomer revealed the characteristic bands of the primary amino group at 3445 and 3355 cm^{-1} (–NH$_2$ stretch), and the nitro group disappeared after the reduction reaction. The NMR spectra were also used to clarify the structures of intermediate compounds and final monomers, as depicted in
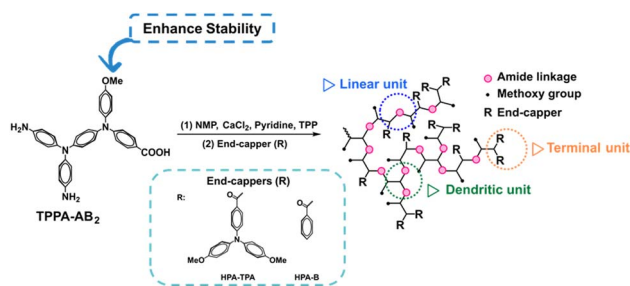
Scheme 1 Design structure and schematic presentation of AB$_2$-type hyperbranched polyamides.

Fig. S3–S8.† The chemical shift assignments indicated that the proton and carbon peaks agreed with the desired compounds. It was found that for the final target monomers, **TPPA-AB₂** and **TPPA-AB**, the characteristic peaks of NH₂ and COOH could not be observed in the ¹H-NMR spectra owing to the strong interaction between the active hydrogen and deuterated solvent, making them non-investigated. Nevertheless, the carbonyl group of carboxylic acid for **TPPA-AB₂** and **TPPA-AB** could be found in the ¹³C-NMR spectra at 167.09 and 167.17 ppm, respectively, as shown in Fig. S5 and S8.†

The aromatic hyperbranched polyamides **HPA-TPA** and **HPA-B** were prepared by direct polycondensation of **TPPA-AB₂** with the incorporation of the end-capping agents of 4-carboxy-4′,4″-dimethoxytriphenylamine and benzoic acid (**TPA** and **BA**), according to the previously reported methods by Kakimoto *et al.*[18] The detailed polymerization conditions of **HPA**s and **LPA** were described in the ESI† and are summarized in Scheme S2.† In the FT-IR spectra of the three polyamide films shown in Fig. S15,† **LPA** exhibited characteristic absorption bands of the amide group at 3315 cm⁻¹ (–NH stretching) and 1665 cm⁻¹ (amide carbonyl stretching). For the prepared hyperbranched polyamides, both **HPA-B** and **HPA-TPA** featured amide bands at 3310 cm⁻¹ (–NH stretching) and 1645 cm⁻¹ (amide carbonyl stretching), confirming the end-capping reaction. The resulting polyamides showed inherent viscosities ranging from 0.27 to 0.47 dL g⁻¹, and the weight-average molecular weights (M_w) and polydispersity index (PDI) were within the range of 67.2 to 41.6 kDa and 1.9 to 2.3, respectively, as tabulated in Table S1.† Although the prepared **HPA-TPA** and **HPA-B** revealed lower inherent viscosities than that of the linear **LPA**, the M_w values of the hyperbranched polymers were comparable or higher than that of **LPA** due to their extensively branched structure-causing low-viscosity characteristics.[38,39] The resulting HPAs demonstrated excellent solubility in common organic solvents, as tabulated in Table S2.†

Besides, to prove the hyperbranched architectures of **HPA-TPA**, the Mark–Houwink equation ($[\eta] = KM^{\alpha}$) was used to investigate. According to the reference, this curve is precisely in line with the characteristics of hyperbranched polymers.[40] Based on the slope of the linear fit obtained through the least-squares method, the α value of **HPA-TPA** was estimated at around 0.50, indicating a highly branched structure, as depicted in Fig. S16.† Furthermore, these hyperbranched polymers comprising linear (L), dendritic (D), and terminal (T) units are illustrated in Fig. 1a and S17.† The degree of branching (DB) is a critical factor in the analysis of the hyperbranched polymers, defined as the ratio of the sum of D and T units to the total units (L, D, and T units), which could be estimated using the equation $DB = (D + T)/(L + D + T)$.[41] The determination of DB was done by employing ¹H NMR of the amide peak of **HPA-TPA** for analysis, the deconvolution method was applied to separate the overlapping amide peaks for the terminal (H_T), linear (H_{L_1}, H_{L_2}), and dendritic (H_D) units, and their chemical shifts were defined at 9.96, 9.94, 9.93, and 9.92 ppm, respectively. As shown in Fig. S17,† in the first 30 minutes of polymerization, the L units (L_1 and L_2) contributed the most to the integrated value (58.8%). In contrast, the D unit contributed less, with a DB value of around 0.41. After that, the contribution percentage of the D unit progressively increased, whereas the contribution of the L units gradually decreased along with the polymerization time to 100 min, and the DB value increased from 0.41 to 0.57, as summarized in Table S3,† implying that the prepared polyamides have a highly branched architecture.

Thermogravimetric analysis (TGA) and differential scanning calorimetry (DSC) were performed to examine the thermal behaviours; the representative curves are depicted in Fig. S18 and S19,† and the results are summarized in Table S4.† All the resulting polyamides demonstrated remarkable thermal stability, displaying T_d^5 higher than 400 °C under nitrogen and air atmospheres. The glass-transition temperatures (T_g) of **HPA-TPA**, **HPA-B**, and **LPA** polyamides were 213, 232, and 238 °C, as shown in Fig. S19.† **HPA-TPA** exhibited the lowest T_g compared to the linear polymer **LPA** owing to the more free volume generated in the intensively hyperbranched polymer structure.[42]

Microporous properties of the polyamides

According to the results of T_g, we suppose that **HPA-TPA** should contain more free volume in the polymer matrix; thus, evaluating the microporous-related properties is essential. First, the density of the resulting polyamides was measured using a Mettler Toledo scale density kit and 2,2,4-trimethylpentane. **LPA** (1.218 g cm⁻³) displayed a higher density than that of **HPA-B** (1.130 g cm⁻³) and **HPA-TPA** (1.089 g cm⁻³) because of the loose packing within the hyperbranched polymer matrix, causing more free volume. Moreover, introducing the end-capped agent with triphenylamine (TPA) units could lower the density. In addition, the specific surface areas (S_{BET}) of the obtained polyamides were determined using nitrogen adsorption/desorption isotherms by Brunauer–Emmett–Teller (BET) theory at a temperature of 77 K, as illustrated in Fig. 1b. The results revealed that **HPA-TPA** (27.05 m² g⁻¹) and **HPA-B** (19.95 m² g⁻¹) have higher S_{BET} than that of the linear polyamide **LPA** (5.49 m² g⁻¹). Furthermore, when compared the distribution of pore sizes calculated by the Horvath–Kawazoe method utilizing the nitrogen adsorption/desorption isotherm (Fig. 1c), it was found that the hyperbranched structures could generate more amount of micropores within the polymer matrix than the linear **LPA**.[7,24] The results also demonstrated that the bulky end-capper in **HPA-TPA** could effectively facilitate the formation of intrinsic microporosity. Moreover, wide-angle X-ray diffraction (WXRD) patterns were employed to investigate the d-spacing of the polymer packing, as shown in Fig. 1d. The diffraction patterns of all polymers displayed a broad peak at approximately 17–19°, implying the presence of ordered regions within the amorphous polymer matrix. The calculated d-spacing values from the WXRD analysis, as summarized in Table 1, were 4.62, 4.75, and 5.16 Å for **LPA**, **HPA-B**, and **HPA-TPA**, respectively. This discrepancy arises primarily from the influence of branched structures, which restricted the interchain hydrogen bonding interaction, disrupting the close and orderly conformation of polymer chains. As a result, the disorderly characteristics of polymer chains induce a larger d-spacing among them, thereby generating more inefficient interchain packing within the polymer matrix.[43]
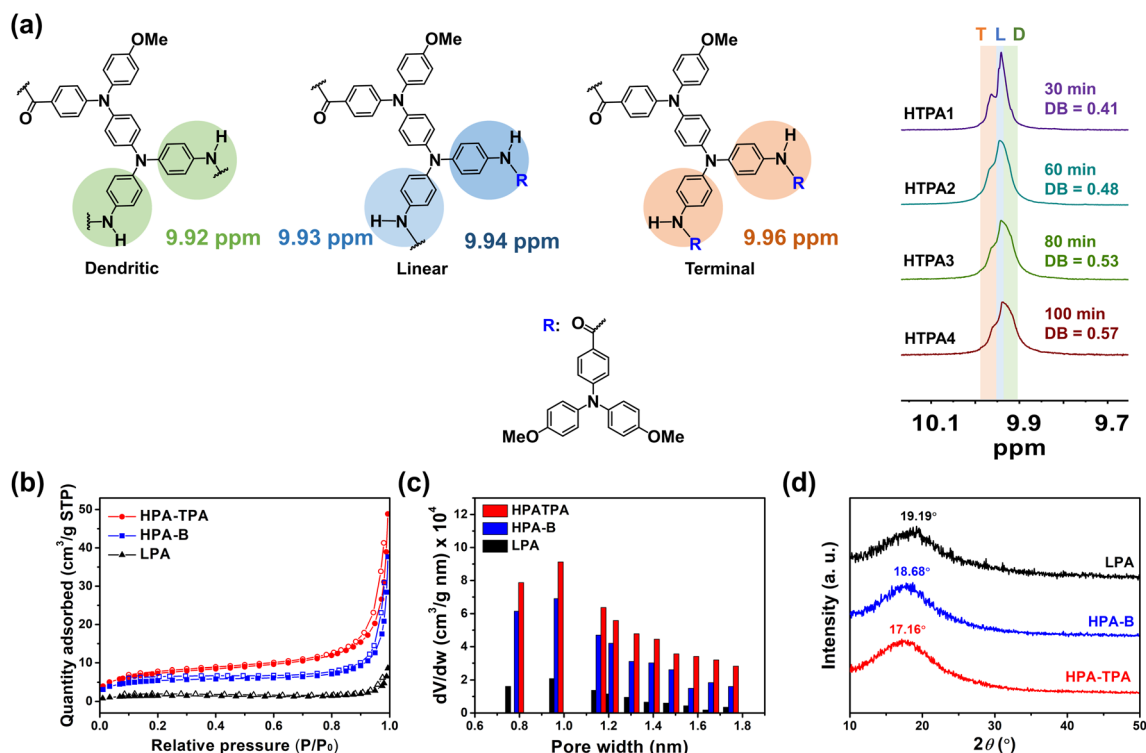
Fig. 1 (a) Degree of branching of **HPA-TPA** with the polymerization time. (b) N$_2$ adsorption and desorption isotherms measured at 77 K. (c) Pore width distribution was analysed through nitrogen adsorption at 77 K *via* the Horvath–Kawazoe method. (d) WXRD patterns of the polyamide films (thickness: 25 ± 5 μm).

Table 1 Porosity parameters of hyperbranched and linear polyamides

Polymer	ρ [g cm^{-3}]	S_{BET}^{a} [m^2 g^{-1}]	$2\theta^b$ [°]	d-spacing^c [Å]
LPA	1.218	5.49	19.19	4.62
HPA-B	1.130	19.95	18.68	4.75
HPA-TPA	1.089	27.05	17.16	5.16

^{a} Calculated by the results of the N$_2$ adsorption (filled) and desorption (empty) isotherms measured via BET analysis at 77 K. ^{b} Measured via XRD analysis at a scan (2θ) ranging from 10 to 50°. ^{c} Calculated from the results of the WXRD curve by applying Bragg's Law.

Electrochemical properties of the polyamide films

Cyclic voltammetry (CV) and differential pulse voltammetry (DPV) were performed to evaluate the electrochemical performance of the redox-active polyamide films, and the preparation of the polymer thin films is described in the ESI.† The resulting polyamides revealed similar oxidation potentials, **HPA-TPA** ($E_{oxi.}$ = 0.75 V), **HPA-B** ($E_{oxi.}$ = 0.78 V), and **LPA** ($E_{oxi.}$ = 0.77 V), due to the similar electroactive structures, as shown and tabulated in Fig. 2a–2c and Table 2, respectively. According to a previous report, the tetraphenyl-*p*-phenylenediamine (TPPA) units exhibited two distinct oxidation potentials.[44] As a result, **HPA-TPA** should have three oxidation potentials owing to the other electroactive site on the TPA end-capping. However, only two significant oxidation potentials were observed in the CV or DPV diagrams, as depicted in Fig. 2a and S20a.† When confirming the DPV diagram in depth, **HPA-B** and **LPA** showed two

similar current responses between the first and second oxidation peaks. Yet, the second oxidation peak of **HPA-TPA** manifested a more significant current response than the first one.

Consequently, the Nernst equation was employed to validate the electron transfer mechanism at each oxidation stage of **HPA-TPA**. The electron transfer number (n) could be estimated through a sequential application of continuous potentials ($E_{applied}$) and an analysis of the concentration ratio between the oxidized and neutral forms ($[O]/[N]$) of the polyamide film, as shown below:[44–49]

$$E_{applied} = E^0 + \frac{0.059}{n}\log\left(\frac{[O]}{[N]}\right)$$

E^0 refers to the standard potential in this equation, and $E_{applied}$ is the applied potential. The value 0.059 represents the resulting ratio of the gas constant, Faraday's constant, and the temperature (K). Notably, $[O]$ and $[N]$ could be transferred to the absorbance of the oxidized ($A_n - A_0$) and neutral ($A_{max} - A_n$) forms by the Beer–Lambert law, respectively, where A_0 is the absorption in its natural state, A_{max} indicates the absorption in the fully oxidized state, and A_n represents the equilibrium absorption for the applied potential. Each spectrum could be recorded after reaching equilibrium at each potential, as shown in Fig. S21–S23.† As tabulated in Table S5,† the calculated n value of **HPA-TPA** exhibited a two-electron-transfer process from 0.82 V to 1.12 V. In contrast, **HPA-B** and **LPA** only performed a one-electron-transfer process from 0.84 to 1.00 V and 0.86 to
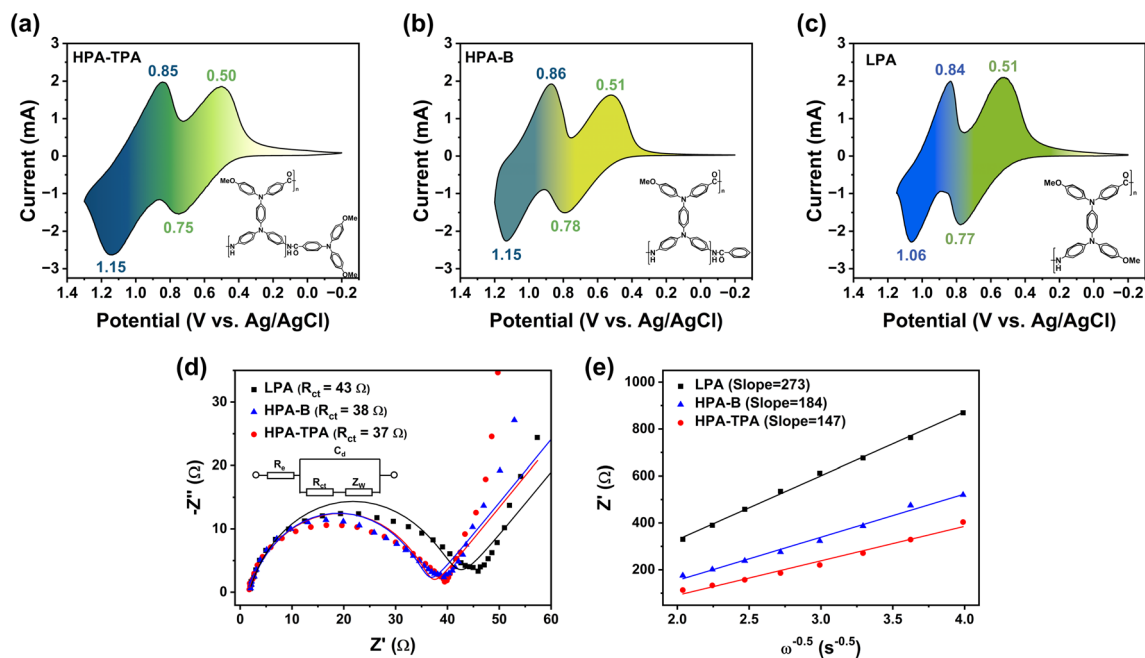
Fig. 2 Cyclic voltammetric diagrams of (a) **HPA-TPA** (thickness: 310 ± 30 nm), (b) **HPA-B** (thickness: 300 ± 20 nm), and (c) **LPA** (thickness: 300 ± 20 nm), measured on the ITO-coated glass substrate (coated area: 0.6 cm × 3 cm) in 0.1 M TBABF$_4$/MeCN at a scan rate of 50 mV s^{-1}. (d) Nyquist plots fitting with Randles equivalent circuit (solid lines are the fitted lines) and (e) the fitted linear plot between Z' and $\omega^{-0.5}$ in the low-frequency region under the oxidation state of the prepared polymer films.

Table 2 Electrochemical behaviours of the prepared polyamide films

| Polymer[a] | 1st oxidation state | | 2nd oxidation state | | R_{ct} [Ω] | σ_w^d [Ω cm^2 s$^{-0.5}$] | D^e [cm^2 s^{-1} 10^{-17}] |
	$E_{oxi.}^b$ [V]	$E_{red.}^c$ [V]	$E_{oxi.}^b$ [V]	$E_{red.}^c$ [V]			
LPA	0.77	0.51	1.06	0.84	43	273	3.3
HPA-B	0.78	0.51	1.15	0.86	38	184	7.3
HPA-TPA	0.75	0.50	1.15	0.85	37	147	11.4

[a] Thickness: **LPA** (300 ± 20 nm), **HPA-B** (300 ± 20 nm), and **HPA-TPA** (310 ± 30 nm). [b] Oxidation potential at the peak at a scan rate of 50 mV s^{-1}. [c] Reduction potential at the peak at a scan rate of 50 mV s^{-1}. [d] Warburg coefficient-slope for the plot of Z' vs. the lower angular frequencies ($\omega^{-0.5}$). [e] Diffusion coefficient of the counter ions, as following equation $D = 0.5 \left(\frac{RT}{ACF^2\sigma_w} \right)^2$, where A stands for the electrode surface area (0.6 cm × 2 cm), C signifies the molar concentration of counter ions, F is Faraday's constant, R is the symbol for the gas constant, and T represents the temperature.

1.02 V, respectively. Furthermore, the characteristic IV-CT absorption peak of the TPPA unit in the **HPA-TPA** backbone at 1000 nm did not decrease along with the applied higher potentials, as shown in Fig. S21c,† implying that the electron transfer from 0.84 to 0.94 V should be attributed to the redox-active TPA end-capping unit.

Electrochemical impedance spectroscopy (EIS) is frequently employed to clarify the electrode resistance for the interfacial charge transfer and mass transport effects.[46] The Randles equivalent circuit was used to analyse impedance (R_{ct}) in this work, and the Warburg coefficient σ_w could be obtained in the low-frequency region to estimate the diffusion coefficient (D).[46,47] The results are illustrated in Fig. 2d, e, and Table 2, respectively. Hyperbranched polyamides, **HPA-TPA** (37 Ω) and **HPA-B** (38 Ω), exhibited similar R_{ct} values but were still smaller than the linear **LPA** (43 Ω). With the same trend, the calculated

diffusion coefficients also suggested that the hyperbranched architecture of **HPA-TPA** (11.4 cm^2 s^{-1} 10^{-15}) and **HPA-B** (7.3 cm^2 s^{-1} 10^{-15}) facilitates the higher counter anion (BF$_4^-$) mobility than the **LPA** (3.3 cm^2 s^{-1} 10^{-15}) owing to the inefficient packing of the polymer chains. According to the results analysed from microporosity and electrochemistry, the hyperbranched polyamides could be expected to perform remarkably electrochromic behaviours.

Electrochromic properties of the polyamide films and devices

Spectroelectrochemical measurements were conducted to elucidate the electrical stimuli to the optical response of resulting polyamides throughout the redox process. The characteristic absorption patterns and the corresponding color appearance of **HPA-TPA**, **HPA-B**, and **LPA** films at different applied potentials are depicted in Fig. 3a, S24a, and S24b,†
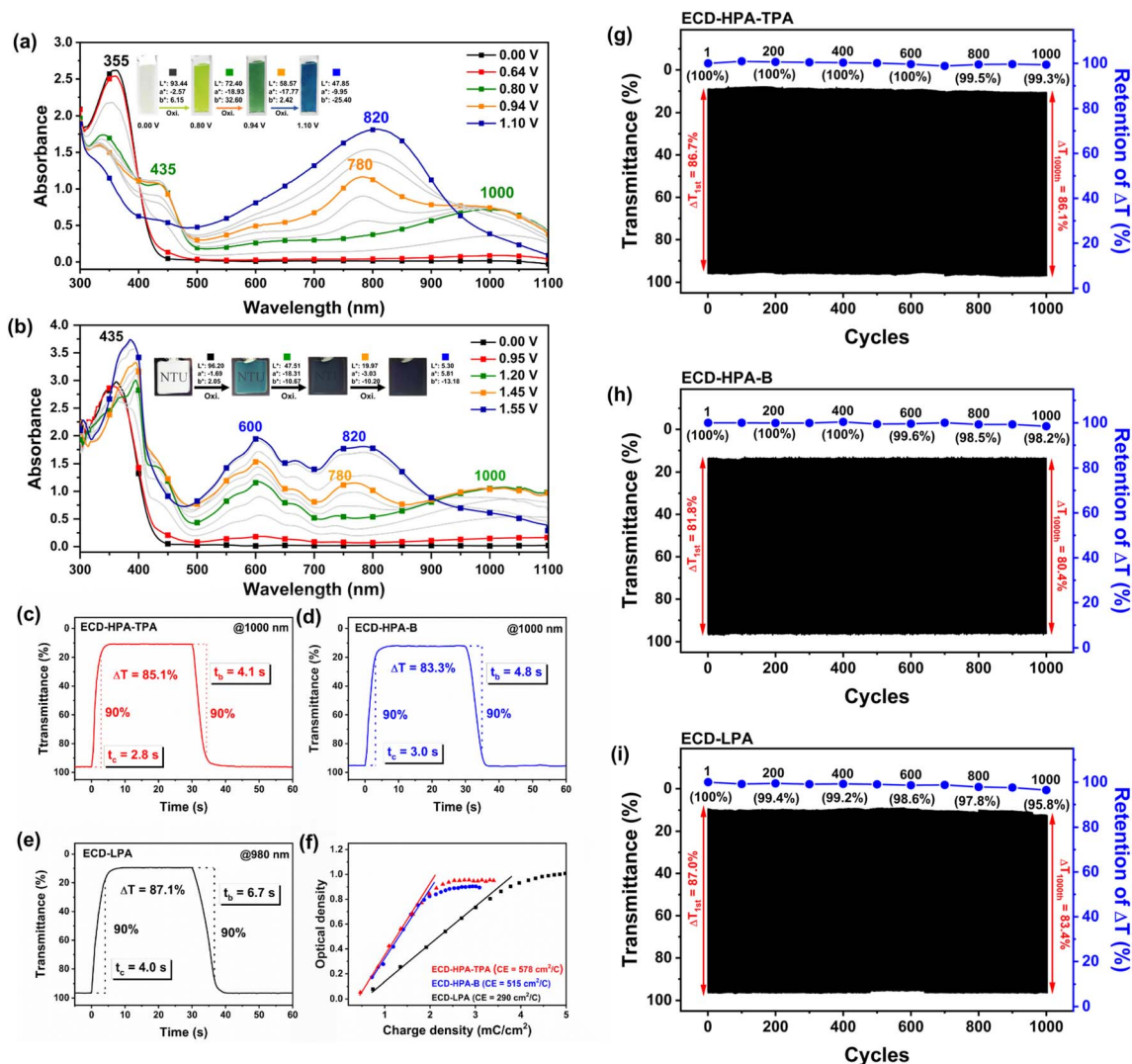
Fig. 3 Spectroelectrochemical spectra and the analysis of CIELAB colour space for (a) **HPA-TPA** (thickness: 310 ± 30 nm) and (b) **ECD-HPA-TPA** (thickness: 330 ± 30 nm). Response time and switching stability of ECDs (c and g) **ECD-HPA-TPA** (thickness: 260 ± 30 nm), (d and h) **ECD-HPA-B** (thickness: 270 ± 30 nm), and (e and i) **ECD-LPA** (thickness: 250 ± 30 nm) between −0.3 and 1.2 V at a cycle time of 60 s on the ITO-coated glass substrate (coated area: 2 cm × 2 cm) in about 5 mL propylene carbonate with 0.1 M TBABF$_4$ and 0.015 M HV(BF$_4$)$_2$ as electrolytes. (f) Optical density *vs.* charge density ECDs of **HPA-TPA** at 1000 nm, **HPA-B** at 1000 nm, and **LPA** at 980 nm in the coloration process to obtain coloration efficiency by the fitting slope. For the switching stability test, applied potentials were set to −0.3 V (OFF) and 1.2 V (ON) with a cycle time of 60 s on the ITO-coated glass substrate.

respectively. In the neutral state (0 V), all the prepared polyamide films were highly transparent with pale yellow color, displaying notable absorption at approximately 355 nm, which is assignable to the π–π* transition between the aromatic ring and the electroactive nitrogen centre. After undergoing the first oxidation potential (0.80 V), the films appeared yellow-green, increasing absorption at around 435, 600, and 1000 nm for all the prepared polyamides. The broad absorption peak in the near-infrared region (NIR) could be ascribed to the high electron coupling associated with the delocalized mixed-valence class III structure, known as the intervalence charge transfer (IVCT) phenomenon.[48] With the elevation of the potential from 0.80 to 0.94 V in the **HPA-TPA** film, a new absorption band was generated around 780 nm, assigned to

the second oxidation stage and attributed to the end-capped triphenylamine unit as aforementioned in the Nernst analysis section.[49] In the CIE *L*a*b** measurement, the *b** value of **HPA-TPA** decreased from 32.60 to 2.42, displaying a green appearance.

In contrast, as the applied potential increased from 0.80 to 1.10 V, **HPA-B** and **LPA** revealed additional absorption peaks generated at around 800 nm with the decreased IV-CT absorption bands, manifesting the pale verdigris and blue appearance. The disappearance of IV-CT absorption could be attributed to the fully-oxidized TPPA architecture. Thus, IV-CT absorption should also decrease when **HPA-TPA** was applied from 0.94 V to 1.10 V while intensifying a new absorption at 820 nm and transforming the film colour to a blue appearance.

EC switching response capability behaviours of the EC polymer films in their first oxidation state were elucidated by tracking the absorption of characteristic peaks along with time to observe the variation during the redox procedure. The switching response time estimated based on the 90% absorption intensity difference of characteristic peaks of the completed switch for the films of **HPA-TPA**, **HPA-B**, and **LPA** is illustrated in Fig. S25 and S26,† encompassing the electrochemical cycle between 0.8 V (ON) and −0.2 V (OFF) each for 100 seconds. When monitoring at 1000 nm, **HPA-TPA** revealed the shortest response time of 4.3 s for the colouring (t_c) and 1.9 s for the bleaching (t_b) processes. **LPA** took the most extended response times of 7.4 s for t_c and 2.4 s for t_b, respectively, whereas **HPA-B** exhibited t_c of 4.5 s and t_b of 2.2 s. The calculated coloration response speed demonstrated enhancing trends of 10.8% s^{-1}, 16.6% s^{-1}, and 17.6% s^{-1} for **LPA**, **HPA-B**, and **HPA-TPA**, respectively, and the results are summarized in Table S6.† **HPAs** exhibited higher EC response capability than that of the **LPA** in colouring and bleaching processes owing to the highly branched architectures facilitating counter-ion diffusion within the polymer matrix. Thus, the most micropore-containing **HPA-TPA** led to the shortest colouring and bleaching response times. Furthermore, the coloration efficiency (CE) is crucial in evaluating EC materials as switching response time. The definition of coloration efficiency could be $CE = \Delta OD/Q$, where ΔOD represents the optical density, and Q is the total charge consumed per working area unit (C cm^{-2}), as depicted and tabulated in Fig. S25d, S26d, and Table S6,† respectively.[50] The EC performance of the **HPA-TPA** film displayed a notable CE reaching 487 cm^2 C^{-1}, much higher than that of **HPA-B** (435 cm^2 C^{-1}) and **LPA** (295 cm^2 C^{-1}), implying that the highly branched architecture could facilitate a high-energy-efficient EC performance in addition to the response capability.

ECDs derived from **HPA-TPA**, **HPA-B**, and **LPA** films employing liquid-type electrolyte ambipolar systems are depicted in Fig. S27,† including 0.015 M heptyl viologen (HV) as the cathodic EC material and 0.1 M tetrabutylammonium tetrafluoroborate (TBABF$_4$) as the supporting electrolyte in propylene carbonate to evaluate the EC behaviours for substantiating further applications. As reported in a previous study, introducing HV into the device as a complementary EC material could facilitate the resulting device to decrease the working potential and the response time and promote

electrochemical stability.[51–55] The CV diagrams and electrochemical impedance spectroscopy of the prepared ECDs are depicted and tabulated in Fig. S28 and Table S7,† respectively. In Fig. 3b and S29,† the spectroelectrochemical spectra and the corresponding L^*, a^*, and b^* values of **ECD-HPA-TPA**, **ECD-HPA-B**, and **ECD-LPA** during the oxidation processes are presented, respectively. The spectroelectrochemical spectra of ECDs displayed a characteristic absorption peak for HV$^{•+}$ at 600 nm in addition to the same absorption peaks produced in the corresponding EC polyamide films as analysed above. In terms of the switching response characteristics, the **ECD-HPA-TPA** exhibited the shortest response times of 2.8 s for colouring and 4.1 s for bleaching, which were shorter than those of **ECD-HPA-B** (t_c: 3.0/t_b: 4.8 s) and **ECD-LPA** (t_c: 4.0/t_b: 6.7 s) under the applied potentials between 1.2 and −0.2 V for colouring and bleaching, as shown in Fig. 3c–3e, S30,† Tables 3, and S8† consistent with the trend of the polymer films that the intrinsic microporosity of **HPAs** influences the improvement of response capability in ECD systems. The EC behaviour of **ECD-HPA-TPA** also exhibited a much higher CE up to 578 cm^2 C^{-1} at 1000 nm than **ECD-LPA** 290 cm^2 C^{-1} at 980 nm, as shown in Fig. 3f. Additionally, the electrochemical stability of ECDs was examined and illustrated in Fig. 3g–3i. Because of the formation of the microporous structure, which is beneficial for the diffusion performance in EC films during counter ion insertion and extraction, the **HPA** system behaved with high switching stability. **ECD-HPA-TPA** demonstrated outstanding electrochemical stability and retained 99.3% of their switching stability after 1000 cycles each of 30 s between 1.2 and −0.2 V, suggesting a promising applicability.

Capacitive analyses and properties of the hyperbranched polyamide (HPA) films

For evaluating the capacitive behaviour of the redox-active non-conjugated hyperbranched and linear polyamides, the galvanostatic charge–discharge (GCD) technique was used to investigate the charge–discharge profiles, and the calculated C_{sp}, energy density, and power density are tabulated in Table S9.† In Fig. S31,† **HPA-TPA** revealed the highest capacitive contribution compared to the others, attributed to the hyperbranched architecture. At the first oxidation stage, **HPA-TPA** and **LPA** showed specific capacitances (C_{sp}) of 78.9 F g^{-1} at 0.5 A g^{-1} and 125.1 F g^{-1} at 0.5 A g^{-1}, and the C_{sp} value gradually decreased along with the higher charge–discharge current densities, as shown in

Table 3 Electrochromic properties and switching response time of ECDs

Device[a]	λ_{abs}[b] [nm]	ΔT[c] [%]	t_c[d] [s]	t_b[e] [s]	ν[f] [% s^{-1}]	η_{CE}[g] [cm^2 C^{-1}]
ECD-LPA	980	87.1	4.0	6.7	19.6	290
ECD-HPA-B	1000	83.3	3.0	4.8	25.0	515
ECD-HPA-TPA	1000	85.1	2.8	4.1	27.4	578

[a] Thickness: ECD-LPA (350 ± 20 nm), ECD-HPA-B (320 ± 20 nm), and ECD-HPA-TPA (330 ± 30 nm) on the ITO-coated glass substrate (coated area: 2 cm × 2 cm) in 0.1 M TBABF$_4$/PC electrolyte with 0.015 M HV(BF$_4$)$_2$. [b] Observed wavelength at the ON state (1.2 V). [c] Optical contrast ratio is $\Delta T = T_b - T_c$, where T_b and T_c are transmittances of the bleaching and coloring states, respectively. [d] Coloring time from a neutral state to 90% of optical change. [e] Bleaching time from coloring state to 90% of the optical change. [f] Response speed is defined as 90% of ΔT divided by t_c. [g] Coloration efficiency is defined as the slope of the δOD (optical density) vs. Q (charge consumed).
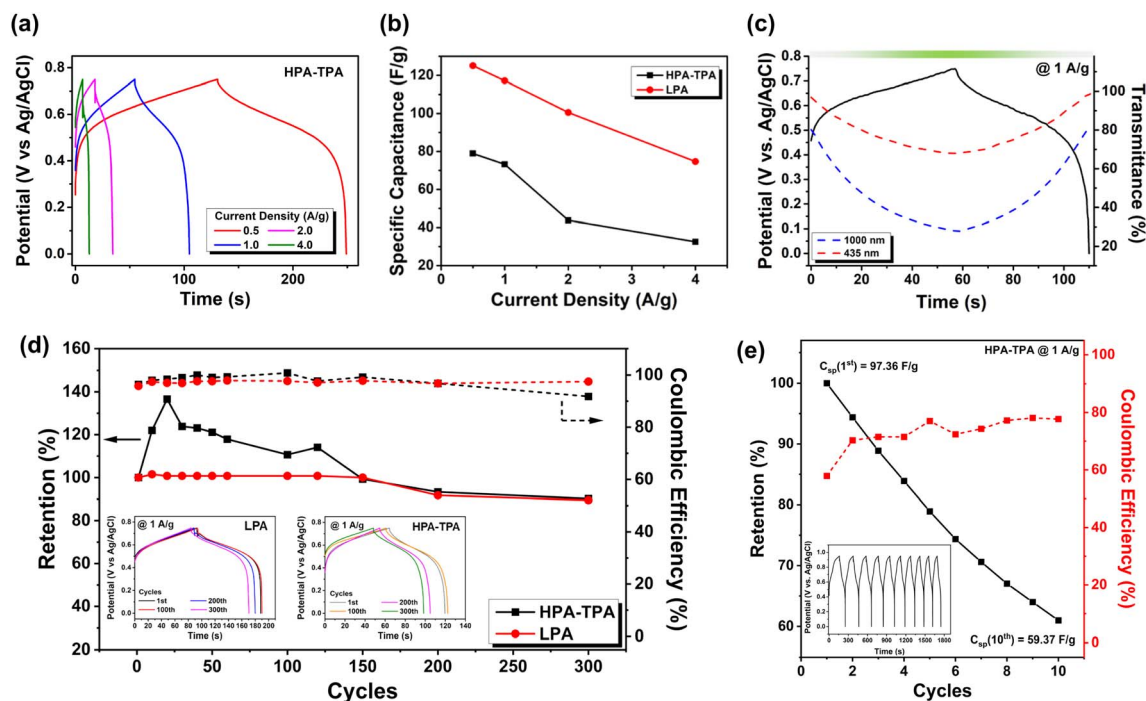
Fig. 4 (a) Galvanostatic charge–discharge (GCD) diagram of **HPA-TPA** (thickness: 220 ± 10 nm) at different applied current densities. (b) Comparison of the specific capacitance of **HPA-TPA** and **LPA** (thickness: 220 ± 20 nm) at different current densities. (c) Transmittance changes *versus* the *in situ* charge–discharge process of **HPA-TPA** at 1.0 A g^{-1}. (d) GCD stability measurements of **LPA** and **HPA-TPA** at 1.0 A g^{-1}. (e) GCD stability measurement of **HPA-TPA** in the second oxidation stage at 1.0 A g^{-1}.

Fig. 4a, b and S32.† Upon the charge–discharge process, the optical transmittance differences at 435 and 1000 nm were more than 50%, which helps monitor the residual capacitance (Fig. 4c). In comparison, **LPA** revealed a higher value of C_{sp}, indicating that the linear structure could perform higher C_{sp} than the hyperbranched one. However, based on the same mass and oxidation stage, only the effective percentage of 61.4% redox TPPA moieties, which could contribute to capacitance within the **HPA-TPA** structure, was lower than that of **LPA**. Thus, if we consider calibrating C_{sp} by the contributed content of **HPA-TPA**, C_{sp} could reveal a comparable value to **LPA**, reaching 119.3 F g^{-1} at 1.0 A g^{-1}. When further evaluating the charge–discharge stability of **HPA-TPA** with a highly hyperbranched architecture, it exhibited gradual increments in the C_{sp} value up to 100.9 F g^{-1} at 1.0 A g^{-1} in the first 20 cycles, increasing to 136.6% retention (Fig. 4d). To our knowledge, the microporous or mesoporous EC supercapacitor materials would initially show an increase in the C_{sp} value due to the longer activation process for the electroactive species in the counter ions.[28,56–58] In contrast, the linear **LPA** exhibited a steady C_{sp} value at the first 150 cycles, implying that **LPA** without the microporous architecture attracts more counter ions to have a longer activation process.

Furthermore, if calibrated by the practical content of the TPPA moiety, C_{sp} of **HPA-TPA** would gradually show up to 164.4 F g^{-1} at the first 20 cycles, implying that the branched architecture was beneficial to the capacitive behaviours. In addition, **HPA-TPA** and **LPA** showed similar stabilities with 90.2% and 89.4% retention, respectively, after 300-cycle charge–discharge

measurements. However, in the second oxidation stage (0.95 V), **HPA-TPA** showed inferior stability and only 60.9% retention after the 10-cycle charge–discharge process. In this stage, the oxidation of the end-capping **TPA** unit started to store the energy, implying that the TPA moiety was unstable for the long-term capacitive measurement. To confirm this issue, **PA-TPAOMe**, a linear-type polyamide, was used to elucidate the long-term capacitive behaviour of the TPA moiety. As depicted in Fig. S33,† when evaluating the charge–discharge stability at 1.0 A g^{-1}, **PA-TPAOMe** revealed only 76.7% and 62.4% retention after 10 and 20 cycles of the GCD process, indicating that the TPA moiety became unstable once the TPA moiety reached the oxidation state upon the charge–discharge process. Meanwhile, the charge–discharge stability could be significantly enhanced when the oxidized triarylamine moiety could resonate with other electroactive centres, such as the IV-CT phenomenon in the TPPA moieties of **HPA-TPA** and **LPA**. When comparing with recent references on different polymeric electrodes, C_{sp} of **HPA-TPA** and **LPA** exhibited moderate values among the reference data, as tabulated in Table S10.† Besides, HPA-TPA and LPA showed better C_{sp} values than that of the listed conjugated polymeric electrodes. In the EC properties, **HPA-TPA** and **LPA** revealed the best optical contrast ratio among the reference data; HPA-TPA especially showed the highest colouration efficiency, resulting from the aid of the hyperbranched architecture. Our future work will further elucidate this phenomenon by comparing structure-related arylamine-based non-conjugated polymers on charge–discharge stability.

Conclusions

An AB$_2$-type hyperbranched polyamide has been successfully designed and synthesized in this work *via* polycondensation with two end-caps to improve the intrinsic microporous features further. The addition of the hyperbranched structure allowed for the formation of more intrinsic microporous materials and improved the electrochromic behaviour by efficiently enhancing the diffusion dynamics of the counter-ions. The electroactive hyperbranched polyamides, **HPA-TPA**, have the most significant intrinsic microporous structures with the largest *d*-spacing (5.16 Å), the lowest density (1.089 g cm^{-3}), and the highest specific surface area (27.05 m^2 cm^{-1}). **HPA-TPA** films with these characteristics further highlight the most remarkable performance features, which include noteworthy contrast ratios, multicoloured electrochromic behaviour, and short switching response times (t_c: 4.3 s/t_b: 1.9 s) for the electrochemical behaviours. When scanning the potentials positively from 0.00 to 1.1 V, the colour changes from the pale yellowish neutral form to the green, dark green, and dark blue oxidized forms. Furthermore, **ECD-HPA-TPA** demonstrated superior response capabilities (t_c: 2.8 s/t_b: 4.1 s) at NIR regions, over the structure-related linear-type **ECD-LPA** (t_c: 4.0 s/t_b: 6.7 s), retaining its advantage even after fabrication into ECDs. It also revealed the highest colouration efficiency (578 cm^2 C^{-1}) and remarkable switching stability for future applications. Furthermore, **HPA-TPA** exhibited a C_{sp} value of 73.2 F g^{-1} at 1.0 A g^{-1} and performed enhanced C_{sp} up to 138% increment in the first 20 cycles than the linear **LPA**, which could only behave as a maintained value.

Data availability

The data supporting this article have been included as part of ESI.†

Author contributions

Y.-J. Shao measured the electrochemical properties and prepared the draft of the manuscript. Y.-J. Cho synthesized the monomers and polymers, measured the basic properties of the resulting polymers, and prepared the manuscript draft. H.-L. Li measured some basic properties. C.-C. Hu provided the instrument for the microporous measurement and revised the manuscript. G.-S. Liou designed the concept and the chemical structures, guided and supervised the project, and revised the manuscript.

Conflicts of interest

There are no conflicts to declare.

Acknowledgements

Notes and references

1 C. Gu, A.-B. Jia, Y.-M. Zhang and S. X.-A. Zhang, *Chem. Rev.*, 2022, **122**, 14679–14721.
2 Y. Zhai, J. Li, S. Shen, Z. Zhu, S. Mao, X. Xiao, C. Zhu, J. Tang, X. Lu and J. Chen, *Adv. Funct. Mater.*, 2022, **32**, 2109848.
3 Q. Huang, J. Wang, H. Gong, Q. Zhang, M. Wang, W. Wang, J. P. Nshimiyimana and X. Diao, *J. Mater. Chem. A*, 2021, **9**, 6451–6459.
4 S. Nundy, A. Mesloub, B. M. Alsolami and A. Ghosh, *J. Cleaner Prod.*, 2021, **301**, 126854.
5 J. Koo, V. Amoli, S. Y. Kim, C. Lee, J. Kim, S.-M. Park, J. Kim, J. M. Ahn, K. J. Jung and D. H. Kim, *Nano Energy*, 2020, **78**, 105199.
6 S. Kandpal, T. Ghosh, C. Rani, A. Chaudhary, J. Park, P. S. Lee and R. Kumar, *ACS Energy Lett.*, 2023, **8**, 1870–1886.
7 K. Yamamoto, D. Suemasa, K. Masuda, K. Aita and T. Endo, *ACS Appl. Mater. Interfaces*, 2018, **10**, 6346–6353.
8 H. J. Yen and G. S. Liou, *Polym. Chem.*, 2018, **9**, 3001–3018.
9 H. J. Yen and G. S. Liou, *Chem. Mater.*, 2009, **21**, 4062–4070.
10 H. S. Liu, B. C. Pan, D. C. Huang, Y. R. Kung, C. M. Leu and G. S. Liou, *NPG Asia Mater.*, 2017, **9**, e388.
11 J. Liu, M. Li and J. Yu, *ACS Appl. Mater. Interfaces*, 2022, **14**, 2051–2057.
12 B. C. Pan, W. H. Chen, S. H. Hsiao and G. S. Liou, *Nanoscale*, 2018, **10**, 16613–16620.
13 M. H. Pai, C. C. Hu, W. S. Tan, J. S. Yang and G. S. Liou, *ACS Macro Lett.*, 2021, **10**, 1210–1215.
14 Y. J. Shao, T. C. Yen, C. C. Hu and G. S. Liou, *J. Mater. Chem. A*, 2023, **11**, 1877–1885.
15 C. R. Yates and W. Hayes, *Eur. Polym. J.*, 2004, **40**, 1257–1281.
16 S. I. Bhat, Y. Ahmadi and S. Ahmad, *Ind. Eng. Chem. Res.*, 2018, **57**, 10754–10785.
17 A.-M. Caminade, A. Beraa, R. Laurent, B. Delavaux-Nicot and M. Hajjaji, *J. Mater. Chem. A*, 2019, **7**, 19634–19650.
18 M. Jikei, K. Fujii, G. Yang and M.-a. Kakimoto, *Macromolecules*, 2000, **33**, 6228–6234.
19 P. J. Flory, *J. Am. Chem. Soc.*, 1952, **74**, 2718–2723.
20 M. S. Belgaonkar and B. Kandasubramanian, *Eur. Polym. J.*, 2021, **147**, 110301.
21 A. Saadati, M. Hasanzadeh and F. Seidi, *TrAC, Trends Anal. Chem.*, 2021, **142**, 116308.
22 Y. Zheng, S. Li, Z. Weng and C. Gao, *Chem. Soc. Rev.*, 2015, **44**, 4091–4130.
23 J. E. Durantini, R. Rubio, C. Solis, L. Macor, G. M. Morales, M. I. Mangione, D. A. Heredia, E. N. Durantini, L. Otero and M. Gervaldo, *Sustainable Energy Fuels*, 2020, **4**, 6125–6140.
24 N. Sun, S. Meng, Z. Zhou, D. Chao, Y. Yu, K. Su, D. Wang, X. Zhao, H. Zhou and C. Chen, *Electrochim. Acta*, 2017, **256**, 119–128.

25 D. Hölter, A. Burgath and H. Frey, *Acta Polym.*, 1997, **48**, 30–35.

26 G. S. Liou, H. Y. Lin and H. J. Yen, *J. Mater. Chem.*, 2009, **19**, 7666–7673.

27 T. G. Yun, X. Chen and J. Y. Cheong, *Batteries Supercaps*, 2023, **6**, e202200454.

28 X. Jiao, G. Li, Z. Yuan and C. Zhang, *ACS Appl. Energy Mater.*, 2021, **4**, 14155–14168.

29 Y. Xie, Y. Zhang, M. Li, R. Huang, X. Liu and D. Chao, *Chem. Eng. J.*, 2023, **470**, 144099.

30 C.-P. Constantin, M. Balan-Porcarasu and G. Lisa, *J. Energy Chem.*, 2024, **91**, 433–452.

31 Q. Liu, X. Ou, Y. Niu, L. Li, D. Xing, Y. Zhou and F. Yan, *Angew. Chem., Int. Ed.*, 2024, **63**, e202317944.

32 Z. Wu, Z. Lian, T. Ding, J. Li, J. Xu, J. Wang, L. Zhang, B. Wang, S. Chen and P. Xiao, *J. Energy Chem.*, 2024, **95**, 86–95.

33 Q. Zhao, Z. Pan, B. Liu, C. Bao, X. Liu, J. Sun, S. Xie, Q. Wang, J. Wang and Y. Gao, *Nano-Micro Lett.*, 2023, **15**, 87.

34 K. Gao, S. Ju, S. Li, S. Zhang, J. Liu, T. Yang, J. Lv, W. Yu and Z. Zhang, *ACS Nano*, 2023, **17**, 18359–18371.

35 C. Wu, H. Shi, L. Zhao, X. Chen, X. Zhang, C. Zhang, J. Yu, Y. Lv, R. Wei and T. Gao, *Adv. Funct. Mater.*, 2023, **33**, 2214886.

36 Y. Xie, M. Li, R. Huang, N. Cao and D. Chao, *Energy Storage Mater.*, 2024, 103321.

37 Y. Xie, J. Chen, M. Zhou and D. Chao, *Dyes Pigm.*, 2023, **212**, 111144.

38 K.-L. Wang, S.-T. Huang, L.-G. Hsieh and G.-S. Huang, *Polymer*, 2008, **49**, 4087–4093.

39 C. J. Hawker and J. M. J. Fréchet, *J. Chem. Soc., Perkin Trans. 1*, 1992, 2459–2469, DOI: 10.1039/P19920002459.

40 G. Yang, M. Jikei and M.-A. Kakimoto, *Macromolecules*, 1999, **32**, 2215–2220.

41 Y. Segawa, T. Higashihara and M. Ueda, *J. Am. Chem. Soc.*, 2010, **132**, 11000–11001.

42 I.-Y. Jeon, H.-J. Noh and J.-B. Baek, *Molecules*, 2018, **23**, 657.

43 D. Chao, L. He, E. B. Berda, S. Wang, X. Jia and C. Wang, *Polymer*, 2013, **54**, 3223–3229.

44 H. J. Yen, S. M. Guo, G. S. Liou, J. C. Chung, Y. C. Liu, Y. F. Lu and Y. Z. Zeng, *J. Polym. Sci., Part A: Polym. Chem.*, 2011, **49**, 3805–3816.

45 L. T. Huang, H. J. Yen and G. S. Liou, *Macromolecules*, 2011, **44**, 9595–9610.

46 A. Yildiz, P. T. Kissinger and C. N. Reilley, *Anal. Chem.*, 1968, **40**, 1018–1024.

47 W. R. Heineman, B. J. Norris and J. F. Goelz, *Anal. Chem.*, 1975, **47**, 79–84.

48 K. Jackowska, A. Kudelski and J. Bukowska, *Electrochim. Acta*, 1994, **39**, 1365–1368.

49 H. B. Andrews and L. R. Sadergaski, *Talanta*, 2023, **259**, 124554.

50 X. Lv, S. Yan, Y. Dai, M. Ouyang, Y. Yang, P. Yu and C. Zhang, *Electrochim. Acta*, 2015, **186**, 85–94.

51 Y. Lu, J. Liang, S. Deng, Q. He, S. Deng, Y. Hu and D. Wang, *Nano Energy*, 2019, **65**, 103993.

52 G. S. Liou and C. W. Chang, *Macromolecules*, 2008, **41**, 1667–1674.

53 H. Murata and P. M. Lahti, *J. Org. Chem.*, 2007, **72**, 4974–4977.

54 M. Fabretto, T. Vaithianathan, C. Hall, P. Murphy, P. C. Innis, J. Mazurkiewicz and G. G. Wallace, *Electrochem. Commun.*, 2007, **9**, 2032–2036.

55 J. T. Wu and G. S. Liou, *Chem. Commun.*, 2018, **54**, 2619–2622.

56 Q. Guo, X. Zhao, Z. Li, B. Wang, D. Wang and G. Nie, *ACS Appl. Energy Mater.*, 2020, **3**, 2727–2736.

57 R. T. Ginting, M. M. Ovhal and J.-W. Kang, *Nano Energy*, 2018, **53**, 650–657.

58 (*a*) S. Halder, S. Garg and C. Chakraborty, *Chem. Eng. J.*, 2023, **470**, 144361; (*b*) G. Zhu, Y. Sun, M. Li, C. Tao, X. Zhang, H. Yang, L. Guo and B. Lin, *Electrochim. Acta*, 2021, **365**, 137373.